STRUCTURAL BIOLOGY

Tracking Ca^{2+} ATPase intermediates in real time by x-ray solution scattering

Harsha Ravishankar[1], Martin Nors Pedersen[2]*, Mattias Eklund, Aljona Sitsel[3†], Chenge Li[4], Annette Duelli[5], Matteo Levantino[2,6], Michael Wulff[2], Andreas Barth[4], Claus Olesen[7], Poul Nissen[3], Magnus Andersson[1‡]

Sarco/endoplasmic reticulum Ca^{2+} ATPase (SERCA) transporters regulate calcium signaling by active calcium ion reuptake to internal stores. Structural transitions associated with transport have been characterized by x-ray crystallography, but critical intermediates involved in the accessibility switch across the membrane are missing. We combined time-resolved x-ray solution scattering (TR-XSS) experiments and molecular dynamics (MD) simulations for real-time tracking of concerted SERCA reaction cycle dynamics in the native membrane. The equilibrium [Ca_2]E1 state before laser activation differed in the domain arrangement compared with crystal structures, and following laser-induced release of caged ATP, a 1.5-ms intermediate was formed that showed closure of the cytoplasmic domains typical of E1 states with bound Ca^{2+} and ATP. A subsequent 13-ms transient state showed a previously unresolved actuator (A) domain arrangement that exposed the ADP-binding site after phosphorylation. Hence, the obtained TR-XSS models determine the relative timing of so-far elusive domain rearrangements in a native environment.

INTRODUCTION

The adenosine 5′-triphosphate (ATP)–dependent transport of Ca^{2+} ions across the sarco/endoplasmic reticulum (SR/ER) membrane restores cytoplasmic calcium levels following calcium signaling. This process is highly active in the termination of muscle contraction and is central to muscle and cardiac physiology (*1*), but also in, for example, secretory (*2*) and neuronal (*3*) tissues. The SR/ER Ca^{2+} adenosine triphosphatase (ATPase) (SERCA) traverses the SR/ER membrane and catalyzes the active cytoplasm-to-SR/ER transport of two Ca^{2+} ions (*4*). Disturbances in SERCA functionality, and hence Ca^{2+} homeostasis, can result in pathological muscle control, such as in heart disease, and perturbed secretory functions (*5*). ATP hydrolysis in the active site located within the cytoplasmic A (actuator), N (nucleotide-binding), and P (phosphorylation) domains and ion binding in the M (membrane) domain shuttle the protein between states of high (E1) and low (E2) ion affinities accompanied by an alternate access to the internal ion-binding sites (Fig. 1). Using inhibitors, ATP analogs, and metallofluorides, SERCA has been trapped and crystallized in intermediate states describing the reaction cycle at an atomistic level (*6*, *7*). The obtained crystal structures show that Ca^{2+} transport is associated with extensive inter- and intradomain rearrangements that couple ATP hydrolysis to ion transport. However, crystal structures show only dynamics at a local spatial scale (*8*, *9*), while large-scale dynamics cause electron density features to fade out, and in addition, key structural intermediates associated with the adenosine 5′-diphosphate (ADP) and Ca^{2+} release are missing (Fig. 1A). Real-time monitoring of SERCA dynamics could possibly resolve transient structural states elusive to known trapping protocols and also answer the fundamental question to what extent the structural rearrangements determined by x-ray crystallography in detergent-lipid mixtures are preserved in the native membrane, which has a highly specific composition of lipids (*10*).

Under normal physiological conditions, the transport cycle [reviewed in (*7*, *11*)] is initiated when the SERCA protein enables access by two Ca^{2+} ions and one ATP molecule to the binding sites in the M and N domains, respectively, thus forming a Ca^{2+}-bound state with a closed cytoplasmic headpiece ([Ca_2]E1ATP) (Fig. 1). The rearrangement of primarily the N domain to approach the P domain sets the stage for autophosphorylation of Asp^{351}, which proceeds through transition ([Ca_2]E1P-ADP) and covalent ([Ca_2]E1P:ADP) states of phosphoenzyme formation. Structural rearrangements in the high-energy [Ca_2]E1P-ADP state infer strain to the A domain, which thereby pulls transmembrane (TM) helices M1–M2 toward the cytoplasm to occlude the Ca^{2+} ions.

Crystal structures corresponding to Ca^{2+}-bound E1 ([Ca_2]E1) and Ca^{2+}-occluded phosphorylated E1 ([Ca_2]E1P-ADP) states have shown that ATP binding and phosphorylation are associated with large structural changes in the cytoplasmic domains going from an open and dynamic to a compact and stable arrangement (*6*, *7*). However, the extent of this structural change has been debated. For instance, it has been suggested that the N domain flexibility is caused by the absence of ATP and therefore is independent of the rest of the protein and that the crystallized open [Ca_2]E1 states represent just a few of the possible states in the presence of Ca^{2+} that might not be dominating, if at all present under physiological conditions with ATP highly abundant in the cytoplasm (*12*). Structures of a Ca^{2+}-free E1 intermediate show a more compact arrangement with an open cytoplasmic pathway leading to the Ca^{2+}-binding sites (*13*, *14*).

The next structurally known reaction cycle intermediate is an outward-open E2P state trapped by BeF_3^- that follows ADP dissociation to the cytoplasm (*6*, *7*). In this state, structural rearrangements of the A domain have induced M1–M6 movements resulting in distorted

[1]Department of Chemistry, Umeå University. Linnaeus Väg 10, 901 87 Umeå, Sweden. [2]European Synchrotron Radiation Facility, Grenoble, Cedex 38043, BP 220, France. [3]DANDRITE–Nordic EMBL Partnership for Molecular Medicine, Department of Molecular Biology and Genetics, Aarhus University. Gustav Wieds Vej 10, 8000 Aarhus C, Denmark. [4]Department of Biochemistry and Biophysics, Stockholm University. Svante Arrhenius Väg 16C, 106 91 Stockholm, Sweden. [5]Department of Biomedical Sciences, University of Copenhagen. Blegdamsvej 3, 2200 Copenhagen, Denmark. [6]Department of Physics and Chemistry, University of Palermo, Viale delle Scienze -Ed 18, 90128 Palermo, Italy. [7]Department of Biomedicine, Aarhus University, Vest Ole Worms Allé 3, 113 8000 Aarhus C, Denmark.
*Present address: X-ray and Neutron Science, Niels Bohr Institute, University of Copenhagen, Universitetsparken 5, 2100 Copenhagen, Denmark.
†Present address: Department of Cellular and Molecular Medicine, KU Leuven, Herestraat 49, 3000 Leuven, Belgium.
‡Corresponding author. Email: magnus.p.andersson@umu.se

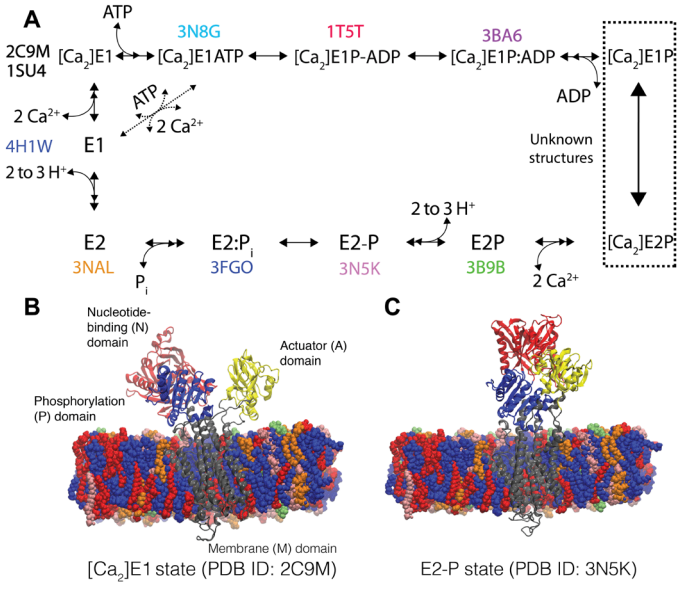

Fig. 1. Principal states involved in SERCA-mediated Ca^{2+} transport. (**A**) Reaction cycle schematic of principal SERCA states and crystal structures (PDB ID) used in the structural refinement. $[Ca_2]$E1P-ADP and $[Ca_2]$E1P:ADP are transition and covalent states of phosphorylation, $[Ca_2]$E1P and $[Ca_2]$E2P are ADP-free phosphorylated states, while E2P, E2-P, and E2:P_i refer to covalent states, hydrolysis transition states, and P_i-bound states of the phosphoenzyme. (**B**) SERCA $[Ca_2]$E1 (PDB ID: 2C9M) and (**C**) E2-P (PDB ID: 3N5K) crystal structures with N (red), P (blue), A (yellow), and M (gray) domains embedded into sarcoplasmic reticulum membrane mimics [consisting of phosphatidylcholine (blue), phosphatidylethanolamine (red), phosphatidylserine (orange), phosphatidylinositol (green), and sphingomyelin (pink) lipids] show the major conformational changes required to achieve the E1-to-E2 transition associated with Ca^{2+} transport.

Ca^{2+} sites exposed to the SR lumen to enable Ca^{2+} release. Hence, there is currently a gap in structural knowledge associated with the accessibility switch across the membrane. Structures of Ca^{2+}-occluded $[Ca_2]$E1P and $[Ca_2]$E2P states associated with ADP release (at that stage ADP-sensitive) and initiation of calcium release to the SR lumen leading to the ADP-insensitive E2P state are so far unknown. These intermediates, however, have been observed from, e.g., biochemical (*15*) and fluorescence microscopy data (*16*). The remainder of the reaction cycle proceeds through E2 states associated with protonation by 2-3 H^+ (E2-P) and dephosphorylation (E2:P_i and E2) that ultimately leads back to an E1 conformation and proton release to the cytoplasm.

The SERCA reaction cycle kinetics and dynamics are highly dependent on temperature and sample conditions. For example, time-resolved studies isolating partial reactions have suggested the rate-limiting steps in the SERCA reaction cycle to be the E1P–E2P transition (*17*) or the reformation of the E1 state after E2P dephosphorylation (*18*), i.e., the inward-outward or the outward-inward transitions relative to the membrane depending on the sample condition used. Hence, selecting experimental conditions that accumulate a rate-limiting state in the E1P–E2P transition could, in principle, enable structural methods that probe conformational change in real time to provide structural information on the elusive Ca^{2+}-bound, phosphorylated intermediates, if triggered into a concerted activity. In addition, because rabbit fast-twitch skeletal muscle SR membranes are constituted by SERCA to >90% of the total protein content (*19*), this characterization of protein dynamics can be performed directly in the native environment.

In early grazing x-ray incidence diffraction studies, laser-induced ATP release from caged ATP [ATP γ-(1-[2-nitrophenyl]ethyl) ester] was used to trigger synchronization of SERCA reaction cycles, which enabled detection of a reaction intermediate corresponding to a phosphorylated Ca^{2+}-bound state within a single-cycle turnover (*20*). In the same study, a similar $[Ca_2]$E1P state was observed to accumulate under steady-state conditions, which indicates that the E1P–E2P transition can be the rate-limiting step in the Ca^{2+} transport reaction cycle. However, lamellar diffraction experiments on partially dehydrated SR multilayers can only resolve profile differences perpendicular to the membrane normal, while solution-scattering studies in principle enable modeling of three-dimensional envelopes of protein structures.

The time-resolved x-ray solution scattering (TR-XSS) methodology can be used to characterize subtle structural dynamics in photoactive chemicals (*21*), protein dimerization (*22*), and for tracking of conformational changes of soluble proteins (*23*–*26*), as well as membrane proteins in detergent micelles (*8*, *27*) and nanodiscs (*28*). A hybrid approach capable of resolving both local and global structural rearrangements has also been proposed (*29*). In these pump-and-probe experiments, a pump laser pulse is typically used to trigger the desired reaction followed by the x-ray probe pulse. Insertion devices at third-generation synchrotrons can deliver 10^{10} photons onto the sample in a ~100-ps single x-ray pulse (*30*). The intensity of the probe pulse can be boosted by selecting microsecond-long trains of single x-ray pulses. This enhances signal-to-noise and is suitable for tracking structural dynamics of complex biological macromolecules that typically react on the micro- to millisecond time scale.

In this work, we used the TR-XSS methodology to track SERCA structural dynamics between 20 μs and 200 ms following laser-induced photolysis of caged ATP, thereby covering both single-cycle and steady-state dynamics. The chosen experimental conditions were specific to a $[Ca_2]$E1 starting state. Modeling of the TR-XSS prepulse state suggested a compact arrangement of the cytoplasmic domains in solution compared with $[Ca_2]$E1 crystal structures. Kinetic analyses of the structural dynamics following photolysis of caged ATP were consistent with two transitions with rise times of a transient state at 1.5 ms (intermediate state) and buildup of a steady state at 13 ms (late state). The intermediate state showed domain rearrangements consistent with ATP binding and phosphorylation of an E1 state. The late state showed an extensive A domain rotation toward an E2P position, but with the P, N, and M domains remaining largely in the E1 locations. This conformation exposes the ADP-binding site. Hence, the TR-XSS model of the late state describes a hitherto unobserved structure that corresponds to an ADP-sensitive $[Ca_2]$E1P state.

RESULTS

Monitoring SERCA reaction dynamics in real time

To identify transient SERCA states, we tracked single-cycle dynamics and steady-state accumulation in the SERCA reaction cycle by monitoring x-ray scattering from 20 μs to 200 ms after laser photolysis of caged ATP. Difference spectra were obtained by subtracting a spectrum recorded 50 μs before the laser flash (fig. S1, A and B). The resulting difference data contained features originating from rearrangements involving secondary and tertiary structural elements

as well as in the surrounding SR membrane. Negative and positive features at 0.04 and 0.09 $Å^{-1}$, respectively, became discernable at 5 ms (Fig. 2A), which is in agreement with observed rates of ATP release from caged ATP (*31*). In addition, a negative feature was observed at 0.12 $Å^{-1}$ and two weaker positive peaks at 0.16 and 0.22 $Å^{-1}$, respectively (fig. S1B). The data did not differ notably after a time delay of 50 ms, which coincides with the reaction cycle duration under similar conditions (*32*), and indicate accumulation of a state with a rate-limiting decay for time delays >50 ms. Addition of thapsigargin inhibitor, which traps the protein in the E2 state (*33*), completely eliminated difference intensities (Fig. 2B).

The temporal development of transient states was best represented by a sequential three-state model (see Materials and Methods). Spectral decomposition extracted three time-independent basis spectra (Fig. 2C) with an early-to-intermediate state rise time of $\tau_1 = 1.5$ ms and an intermediate-to-late state transition of $\tau_2 = 13$ ms (Fig. 2D). Because the early-state basis spectrum was noisy and occurred in the same temporal regime as photoactivation of the caged ATP, we only considered structural interpretation of the intermediate and late basis spectra. Formation of the intermediate state could possibly hold structural information of a transiently formed state during the first reaction cycle. The subsequent late state was defined by a basis spectrum with ~6.5× magnitude of the spectral features relative to the intermediate-state basis spectrum. Hence, we can expect more pronounced structural changes required to form the late state. In addition, while the intermediate state is represented by SERCA proteins in the very first round of reaction cycles, the late state contained time delays up to 200 ms and, hence, also measured steady-state formation accommodating subsequent reaction cycles, which further contributes to the increased magnitude of the late state. At a temperature of 294 K, the τ_2 time scale corresponds to earlier observed rates of phosphorylation of the SERCA protein (*32*, *34*), which is a relatively slow step that initiates the inward-to-outward (E1P to E2P) transition and Ca^{2+} transport across the SR membrane (*32*). A similar temporal evolution of states was also observed in an independent singular value decomposition (SVD) analysis of the time-resolved data that showed presence of a minor component at shorter time delays, followed by a gradual increase of a major component at longer time delays (fig. S1, D and E).

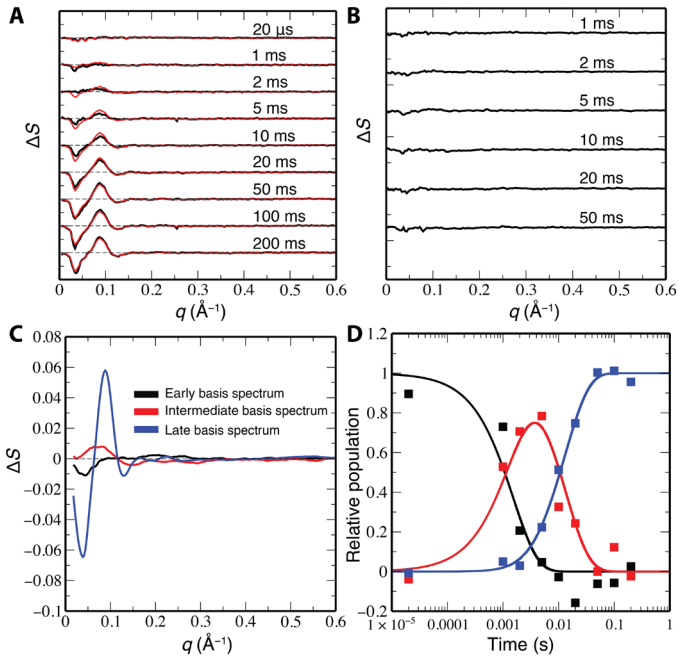

Fig. 2. Monitoring SERCA structural changes and kinetics using TR-XSS. (**A**) Difference x-ray scattering data (black lines) obtained by subtracting dark references (−50 µs) from measurements recorded 20 µs to 200 ms after the laser trigger. The reconstituted data (red lines) resulting from linear combination of the basis spectra and corresponding population densities obtained from the kinetic model [see (**C**) and (**D**)] were aligned with the experimental difference scattering curves. (**B**) TR-XSS data for SERCA in the presence of the thapsigargin inhibitor. The *y* axis scale is identical to that in (A). (C) Time-independent basis spectra obtained from the spectral decomposition revealed three transient states: an early state (black), an intermediate state (red), and a late state (blue). (D) Temporal shifts in the population densities of the early (black), intermediate (red), and late (blue) transient states resulting from a global fit of the three basis spectra to the experimental data. The squares show optimal linear combinations at each individual time point.

Comparison of TR-XSS transient states to crystal structure intermediates

To characterize the identified transient states structurally, we first compared the experimental data to XSS difference curves obtained by subtracting scattering profiles calculated from crystal structures. Because the SERCA-containing membranes in our study were prepared at saturating levels of Ca^{2+} ions (see Materials and Methods) and since all the ATP in the sample was locked in photocages, the dominating prepulse state could be assumed to be represented by $[Ca_2]$E1 structures. We also generated difference profiles using linear combinations of E1 and E2 states since small-angle neutron scattering (SANS) data using detergents with deuteration levels optimized to provide an invisible background in a calcium-free D_2O buffer were shown to match best with a linear combination of Ca^{2+}-free E1 and E2 SERCA states in solution (*35*). However, in no case were the linear combinations superior to the fits resulting from assuming $[Ca_2]$E1 [Protein Data Bank (PDB) ID: 2C9M] as sole component in the prepulse solution (table S1), which also is consistent with the experimental conditions with excess Ca^{2+} to saturate the binding sites. Hence, difference XSS profiles were obtained by subtracting the calculated scattering from a Ca^{2+}-bound E1 state (PDB ID: 2C9M) from scattering profiles calculated from each of the SERCA reaction cycle states: $[Ca_2]$E1ATP (PDB ID: 3N8G), $[Ca_2]$E1P-ADP (PDB ID: 1T5T), $[Ca_2]$E1P:ADP (PDB ID: 3BA6), E2P (PDB ID: 3B9B), E2-P (PDB ID: 3N5K), E2:Pi (PDB ID: 3FGO), and E2 (PDB ID: 3NAL).

The calculated difference profiles for E1-state crystal structures were almost identical, which reflect their structural similarities after forming a compact arrangement of the cytoplasmic domains, while the corresponding calculated difference profiles for the E2 crystal structures showed more variation (Fig. 3, A and B). To quantify the agreement between the calculated and experimental difference XSS profiles, we calculated an R-factor, which is analogous to the standard R-factor in protein crystallography (Eq. 6; see Materials and Methods). A scale factor was used to bring experimental readouts to the same scale as calculated difference scattering profiles. Reflecting the larger magnitude of the late basis spectrum, this scale factor was ~6.5× larger for the intermediate basis spectrum. Since this scale factor stems not only from differences in structural change but also from the late state including time delays longer than a single reaction cycle and hence more protein molecules in the rate-limiting conformation, the intermediate- and late-state basis spectra were compared separately to the calculated difference profiles. Normal

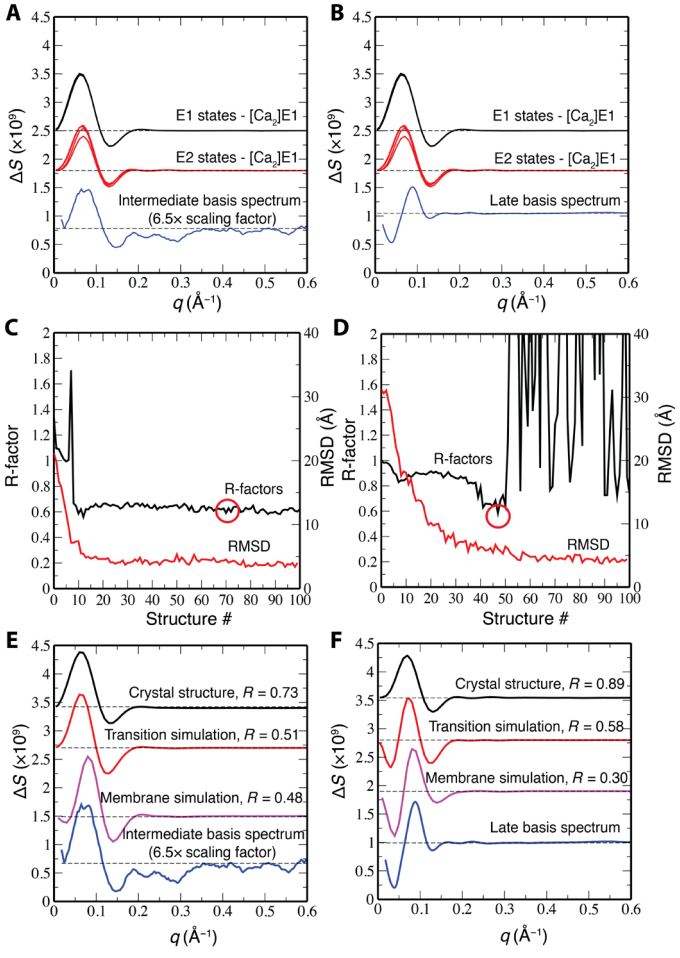

Fig. 3. Structural refinement of the intermediate and late basis spectra. Comparison of TR-XSS (**A**) intermediate and (**B**) late basis spectra to difference scattering profiles generated from subtracting calculated scattering of a $[Ca_2]$E1 crystal structure (PDB ID: 2C9M) from each of the considered E1 (PDB IDs: 3N8G, 1T5T, and 3BA6) and E2 (PDB IDs: 3B9B, 3N5K, 3FGO, and 3NAL) state crystal structures. Simulated transition dynamics from a $[Ca_2]$E1 crystal structure (PDB ID: 2C9M) to the target state (**C**) $[Ca_2]$E1ATP (PDB ID: 3N8G) or the target state (**D**) E2-P (PDB ID: 3N5K). Plotted is the RMSD (red) to each target structure and the corresponding R-factor (black) with respect to the (C) intermediate and (D) late basis spectra. Simulation frames corresponding to the lowest R-factors are encircled (red). Improvements in the best fits to the (**E**) intermediate (with a 6.5× scale factor relative to the late basis spectrum) and (**F**) late basis spectra are shown for difference profiles calculated from crystal structures (black), transition simulation (red), and membrane simulation (magenta).

thermal fluctuations of the SERCA protein simulated at 294 K resulted in an R-factor of 0.1 (see Materials and Methods), which can be considered a minimum possible value or perfect fit to experimental data.

Comparing the late state to the crystal structure difference profiles yielded unsatisfactory R-factors of ~0.9 (table S2). The intermediate state, however, resulted in ~0.2 lower R-factors, which suggest that the domain arrangement in the intermediate state is more reminiscent of those observed in crystallography, while the domains in the late state are combined in a so-far unobserved arrangement. The features in the late-state TR-XSS spectrum not observed in the crystal structures were a pronounced **q** shift of the peak at 0.08 $Å^{-1}$ and its relative size compared with the remaining features, and a feature at $\mathbf{q} < 0.05$ $Å^{-1}$ (Fig. 3B).

Simulation of transition dynamics

To explore whether the transient TR-XSS intermediates could be explained by structural dynamics beyond the crystal lattices, we first simulated transition dynamics between crystal structures using targeted molecular dynamics (MD) simulations without lipids. Protein structures were extracted along the trajectories starting from a $[Ca_2]$E1 state, represented by the 2C9M crystal structure, to each of the seven investigated crystal structure intermediates (fig. S1, F and G). Simulated transition structures toward E1 crystal structures showed R-factor drops from ~0.7 to ~0.5 when compared with the intermediate basis spectrum with root mean square deviations (RMSDs) <5 Å toward the target structures (Fig. 3C and fig. S2). Comparing the E1 transitions to the late-state basis spectrum yielded higher R-factors, with the best R-factors occurring at transition RMSDs >15 Å. We conclude that the intermediate state, but not the late state, can be explained by a closing movement of the cytoplasmic domains, which is the first major structural transition expected following photolysis of the caged ATP for SERCA binding. Reflected by the E1-state structural similarities, the three considered E1 structures resulted in almost identical R-factor scores (table S2). Because the $[Ca_2]$E1ATP state is encountered first in the SERCA reaction cycle, we consider the structure producing the lowest R-factor in this transition as a candidate for further structural refinement of the intermediate state (encircled in Fig. 3C). The agreement between the obtained TR-XSS spectra was improved with a reduction of the positive feature at 0.08 $Å^{-1}$ relative to the negative feature at 0.15 $Å^{-1}$, resulting in a reduction in the R-factor from 0.73 to 0.51 (Fig. 3E). Decomposition of reaction cycle dynamics into consecutive steps using known crystal structures results in peaks at 0.07 and 0.14 $Å^{-1}$ in going from a $[Ca_2]$E1 to a $[Ca_2]$E1ATP state, which indicates that these features represent closure of the cytoplasmic domains upon ATP binding (fig. S3B).

The late-state basis spectrum agreed better with E2 transitions where the E2P (PDB ID: 3B9B, a BeF_3 complex mimicking phosphorylation) and E2-P (PDB ID: 3N5K, an AlF_4 complex mimicking dephosphorylation) states resulted in lower R-factors compared to the subsequent E2:P_i (PDB ID: 3FGO, a MgF_4^{2-} complex) and E2 (PDB ID: 3NAL stabilized by a thapsigargin analog) states (Fig. 3D and fig. S4). Minimum R-factors from both the E2P and E2-P transitions originated from protein structures in midtransition toward the target structures (RMSD >7 Å). Major improvements originated from a feature at $\mathbf{q} < 0.05$ $Å^{-1}$, which was not present in any of the difference profiles calculated from crystal structures using a $[Ca_2]$E1 structure as a common prepulse state (Fig. 3F). However, comparison to x-ray scattering contributions from crystal structures at individual reaction cycle steps shows that transition to the E2P state as well as the dephosphorylation event are associated with features at $\mathbf{q} < 0.05$ $Å^{-1}$ (fig. S3B). Hence, the late state could be best explained by previously elusive domain arrangements captured in the transition between the E1 and E2 states.

Simulating the native environment and domain localization in the prepulse $[Ca_2]$E1 state

Because SERCA functionality is dependent on the lipid environment (*36*), we inserted the best-fitting transition protein structures corresponding to the intermediate and late states, as well as a $[Ca_2]$E1

(PDB ID: 2C9M) crystal structure representing a prepulse state, into membranes that were modeled according to the lipid contents of the SR membrane (*10*). In unrestrained MD simulations, the three SERCA structures sampled conformational dynamics solely restricted by the presence of the membrane. From each trajectory, 200 simulated structures were extracted. The intermediate/prepulse and late/prepulse structure pairs that matched best with the corresponding experimental data were identified from R-factor correlation matrices obtained from 40,000 difference scattering profiles generated by subtracting scattering intensities of simulated prepulse structures from those obtained from the intermediate- and late-state simulations. Local R-factor minima at different parts of the simulation trajectories corresponded to similar structural solutions, which illustrates the robustness of the refinement approach (fig. S5). Including a scattering contribution from the surrounding solvent and lipids did not alter the R-factor distribution between trajectories (fig. S6, A to C). Structure pairs resulting in the lowest R-factors were the same whether or not membrane scattering was included, which possibly can be explained by the large conformational changes in the protruding soluble domains of the SERCA protein dominating the difference scattering compared with structural changes in the membrane.

Difference spectra of simulated intermediate and late states showed better agreement to the time-resolved data when generated by subtraction of simulated [Ca_2]E1 structures compared with the 2C9M crystal structure (Fig. 3, E and F, and table S2). Hence, the major population of structures in the prepulse state in solution is not well represented by the 2C9M crystal structure. The structures from the 2C9M simulation that resulted in the lowest R-factor for the intermediate and late TR-XSS states were overall similar (5 Å backbone RMSD) and showed relatively minor rearrangements of the M and P domains (Fig. 4, fig. S5, D and E, and table S3). However, the positions of the A domain and, in particular, the N domain were shifted compared with the crystal structure. This rearrangement resulted in a more compact arrangement of the A and N domains, changing from a 45- to a 29-Å distance between Thr^{171} (domain A) and Lys^{515} (domain N).

Structural interpretation of the intermediate- and late-state TR-XSS models

The MD-based refinement of the intermediate- and late-state TR-XSS models resulted in substantial reduction of the R-factors to 0.48 and 0.30, respectively, and the resulting structures are real-time representations of the SERCA protein in the native environment (Fig. 3 and table S2). The 1.5-ms intermediate state showed limited rearrangements of the P (RMSD, 5.8 ± 0.7 Å) and M (RMSD, 5.7 ± 0.1 Å) domains when compared with the [Ca_2]E1ATP (PDB ID: 3N8G) crystal structure (Fig. 4 and table S3). However, the orientation of the A domain (RMSD, 11 ± 0.8 Å) in particular, but also the N-domain (RMSD, 6.9 ± 3 Å) differed compared with the crystal structure, which can be explained by their inherent flexibility in transition to the next states. Hence, the intermediate TR-XSS model with a 1.5-ms rise time represents an early Ca^{2+}-bound E1 state where the cytoplasmic domains have closed around the ATP substrate with a slightly different orientation of the A and N domains compared with crystal structures.

Refinement of the 13-ms late state resulted in a structure in which the A domain showed no agreement to either E1/E1P- or E2P/E2-state crystal structures, while the N domain agreed better with an E1 orientation (Fig. 4 and table S3). The P and M domains did not show evident trends toward either state. The late state therefore captured SERCA subsequent to moving the A domain partially toward an E2P position but before any substantial movement of the N domain. The domain rearrangements in the late state were therefore considerably more pronounced compared with those in the intermediate state, which is contributing to the observed magnitude difference of the corresponding basis spectra (Fig. 2D). For structural comparison, the crystal structures most closely representing this part of the SERCA reaction cycle, [Ca_2]E1P:ADP (PDB ID: 3BA6) and E2P (PDB ID: 3B9B), were superimposed onto the late-state TR-XSS model. The A domain in the TR-XSS model was located on a rotating axis in-between the [Ca_2]E1P:ADP and E2P crystal structures (Fig. 5A). The nucleotide-binding site in the cytoplasmic domains is open in the E2P crystal structure, while it is occluded in the [Ca_2]E1P:ADP state (*37*) (Fig. 5B). However, the ADP-binding site appears exposed already in the late-state TR-XSS model (Fig. 5C). Compared with the [Ca_2]E1P:ADP structure, the TR-XSS model showed a structural shift of the phosphorylated Asp^{351} and thereby a decrease in the distance to the Thr-Gly-Glu-Ser (TGES) motif from 28 to 18 Å, which is about halfway to the E2P-state position (Fig. 5D). The TM1–TM3 helices were somewhat shifted toward the corresponding E2P positions, but with calcium-coordinating residues in [Ca_2]E1P-ADP configuration and the M domain completely closed to both sides of the membrane (Fig. 5E). Hence, the late-state TR-XSS model likely represents an intermediate state of the [Ca_2]E1P:ADP to E2P transition, which we assume to be the ADP-sensitive, calcium-occluded [Ca_2]E1P state (Fig. 6).

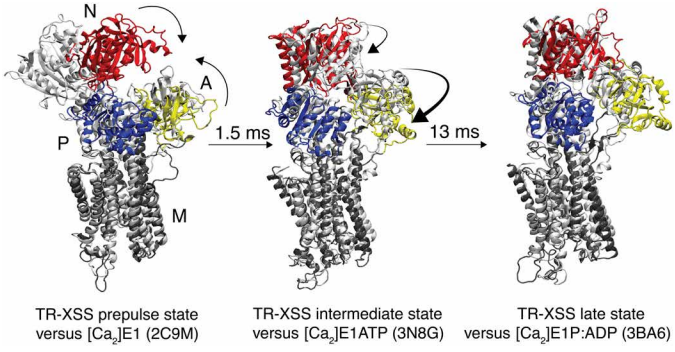

Fig. 4. The refined TR-XSS models of prepulse, intermediate, and late states (N, A, P, and M domains colored as in Fig. 1) are shown with the closest corresponding crystal structures (white) and formation rise times from the kinetic analysis. All protein structures were superimposed on the M7–M10 helices.

DISCUSSION

Membrane proteins carrying out active transport across lipid bilayers are critical to a wide range of cellular processes, such as generation of ion gradients. Because the membrane transporters generally are highly dynamic and show functional dependence on the surrounding membrane, efforts to identify the underlying molecular principles of function and disease should ideally monitor the transport reaction in a lipid environment at room temperature in real time. Given the complexity of the lipid environment and the micro to millisecond time scale on which membrane transporters operate, obtaining direct structural data poses a great challenge and has yet to be standardized. The TR-XSS methodology used in this work registers structural fingerprints in real time that combined with suitable structural refinement

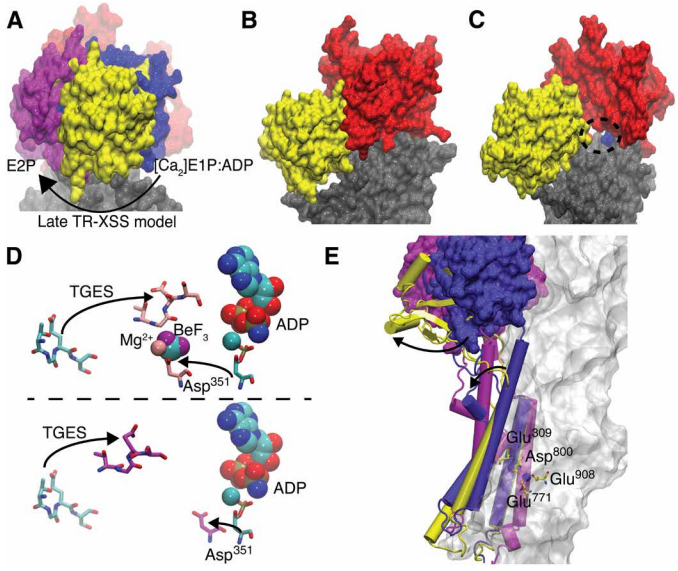

Fig. 5. Real-time dynamics compared with known structural rearrangements. (**A**) Structural differences in the A domain between the late TR-XSS model (yellow), the $[Ca_2]$E1:ADP (PDB ID: 3BA6; blue), and E2P (PDB ID: 3B9B; magenta) states. The N domain is colored red. (**B**) The $[Ca_2]$E1:ADP state crystal structure (PDB ID: 3BA6) displays a closed A-N interface, while in the late-state TR-XSS model, in (**C**), the A domain (yellow) has moved relative the N domain (red) to expose the ADP-binding pocket (encircled). The truncated rest of the ATPase is shown in gray. (**D**) TGES motif and Asp351 dynamics in $[Ca_2]$E1:ADP (PDB ID: 3BA6; cyan) and E2P (PDB ID: 3B9B; pink) (top), and $[Ca_2]$E1:ADP (PDB ID: 3BA6; cyan) and late TR-XSS state (magenta) (bottom). (**E**) TM1–TM3 helices and A domains from $[Ca_2]$E1:ADP (PDB ID: 3BA6), E2P (PDBID: 3B9B), and late state with color coding as in (A) and ion-binding residues from the late state. The truncated rest of the protein is shown as a transparent surface.

approaches can provide structural data of transient intermediates involved in, e.g., membrane transport, along with their kinetics. The structural refinement relies on existence of high-resolution structural data, and the TR-XSS methodology should therefore be viewed as a complementary technique in structural biology that is highly timely since it capitalizes on, e.g., recent developments in cryogenic electron microscopy (cryo-EM).

In this work, we monitored transport dynamics in the SERCA protein following laser-induced access to ATP. The temporal evolution of the difference signals, the extracted rate constants associated with a transient intermediate state, and accumulation of a rate-limiting state are consistent with observed rates of phosphorylation and enzyme turnover (*32*). In the structural refinement procedure, we needed to model a prepulse state to obtain difference data. The chosen experimental conditions with excess Ca^{2+} to saturate SERCA ion-binding sites, but no available ATP, should be best described by a Ca^{2+}-bound E1 state. However, structural features of the $[Ca_2]$E1 state have been debated. Crystal structures of the $[Ca_2]$E1 form (PDB ID: 2C9M or 1SU4) adopt an open conformation of the cytoplasmic domains (*38*) that is in stark contrast to the more compact arrangements found in structures of other SERCA states. Furthermore, the extensive structural rearrangements required for transitioning from open to compact arrangements of the soluble domains are not in agreement with Förster resonance energy transfer that showed no major distance changes in-between the N and P domains in the E1 and E2 states (*12*). The TR-XSS prepulse state model of a $[Ca_2]$E1 state presented here showed a pronounced decrease in the N-A interdomain distance compared with $[Ca_2]$E1 crystal structures (Fig. 4), indicating a predominantly compact conformation of the cytoplasmic domains (see schematic in Fig. 6). However, although the majority of the structural ensemble show a closed arrangement of the cytoplasmic domains, it is likely that more open conformations are also sampled, albeit more rarely (*11*).

Variations of the experimental conditions determine which SERCA state is accumulating at steady state. For instance, a $[Ca_2]$E1P state was observed to dominate in the presence of KCl and high Ca^{2+} concentration (*39*–*41*). Also, using single-molecule fluorescence resonance energy transfer (FRET) microscopy, a Ca^{2+} ATPase from *Listeria monocytogenes* under saturating Ca^{2+} conditions was shown to exhibit a rate-limiting step of phosphorylation and exploit a short-lived calcium-occluded intermediate, which precedes an irreversible step associated with the release of Ca^{2+} ions (*16*). At similar saturating Ca^{2+} conditions, we obtain direct structural information of a state, where unbiased modeling suggests a position of the A domain, which is in-between crystal structures of the $[Ca_2]$E1P-ADP and E2P states, but with the N and P domains still in E1 orientations. In the E2P state, the TGES motif in the A domain has restructured to shield the phosphorylated Asp^{351} from the cytoplasm, thus making the SERCA protein insensitive to possible ADP-induced reverse reactions. In the late TR-XSS conformation, the TGES motif in the A domain has begun its approach toward the phosphorylated Asp^{351} (Fig. 5D), and the ADP-binding site is exposed to the cytoplasm and, hence, primed for ADP release. The refined late TR-XSS state (with a 13-ms rise time) might therefore represent the elusive ADP-sensitive $[Ca_2]$E1P SERCA state, which upon ADP binding can reform ATP from $[Ca_2]$E1P (see schematic in Fig. 6). The trigger releasing the observed dynamics is very likely the completion of the phosphorylation, which in effect breaks a tense configuration of the cytoplasmic domains. The single-molecular FRET studies of *Listeria* Ca^{2+}-ATPase indicate that the protein undergoes very rapid, large-scale conformational changes once phosphorylation has occurred (*16*).

The emerging view that lipids are allosteric modulators of membrane protein function (*42*) calls for efforts in the structural biology field to monitor protein structure and dynamics in the native environment. These studies are often difficult due to the heterogeneity of proteins in the native membranes. The SR membrane constitutes an exception in that it contains >90% SERCA proteins (*19*), enabling structural studies in the native environment. However, accounting for contributions from the surrounding lipid dynamics in TR-XSS experiments is extremely challenging, and no standardized methods currently exist (*8*, *27*, *28*). Because the SERCA cytoplasmic domains protrude substantially from the membrane and display highly dominant conformational changes, the contribution from the surrounding lipids was found to be negligible. To pave the way for characterization of less marked structural changes of proteins lacking protruding movable parts, strategies to deal with the scattering contribution from the surrounding lipids need to be developed.

Last, from a technical point of view, TR-XSS measurements of photoactive chemicals (*21*), photosensitive proteins (*8*, *23*–*28*), and protein dimerization (*22*) paved the way for the data presented in this study. By using laser-induced activation of a caged compound to trigger the transport reaction, our developmental work has enabled extension of the TR-XSS method to include membrane proteins not inherently sensitive to light activation, which drastically increases the number of potential biological targets amenable to the TR-XSS method. In addition, the expected enhanced brilliance in, e.g., the

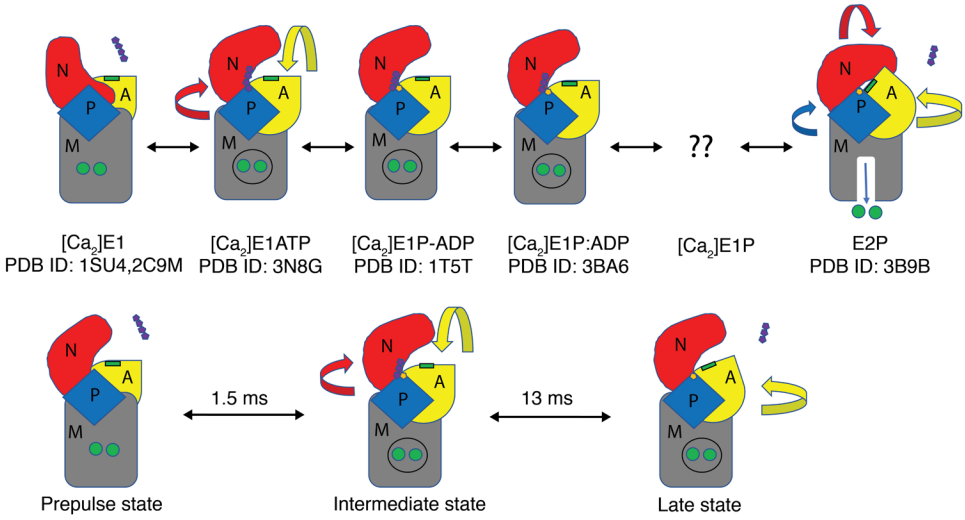

Fig. 6. Schematic comparison of the principal structural rearrangements in-between crystal structures and TR-XSS models. The prepulse state shows reduced opening of the cytoplasmic domains, the intermediate TR-XSS model is similar to a $[Ca_2]$E1ATP state, and displacement of the A domain in the late TR-XSS model exposes the ADP site, but with the N domain not yet in a E2 position. Protein color coding is as in Fig. 1, the ATP and ADP are displayed as four and three purple pentagons, the TGES motif is represented by a green rectangle, the phosphorylated aspartic acid is colored yellow, and the calcium ions are depicted as green circles.

European Synchrotron Radiation Facility (ESRF)–Extremely Brilliant Source (EBS) (Grenoble, France) and MAX IV Laboratory (Lund, Sweden) synchrotrons will further improve signal-to-noise in TR-XSS experiments, thus easing the detection and characterization of transient intermediates in hitherto inaccessible temporal regimes.

MATERIALS AND METHODS

Sarcoplasmic reticulum Ca^{2+} P-type ATPase preparation

SR membranes from rabbit fast-twitch skeletal muscle were prepared according to (*43*) and suspended in buffer containing 150 mM MOPS KOH (pH 7.0), 150 mM KCl, and 75 μM $CaCl_2$ followed by centrifugation at 140,000*g* for 40 min followed by resuspension in the same buffer with the addition of 5 mM $MgCl_2$, 10 mM dithiotrietol, and 10 mM nitrophenyethyl ester (NPE) caged ATP (final concentrations) at a final concentration of 25 mg/ml SR membranes. To avoid disturbance of the native environment, we refrained from detergent extraction of the SERCA protein and, hence, maintained the 90% natural protein purity (*19*).

TR-XSS data collection

The TR-XSS experiments were performed at the dedicated time-resolved beamline ID09 at the ESRF in Grenoble, France (*44*). Because ATP release is an irreversible reaction, purified and concentrated SR membranes containing SERCA were pumped at constant flow rate of 3 μl/min through a 300-μm quartz capillary (Hampton Research), thereby replenishing the sample for each pump-and-probe cycle. NPE-caged ATP in the sample was photolyzed by an Ekspla NT342B nanosecond laser at 355 nm. The laser beam was focused at the sample position in an elliptical 1 mm by 0.25 mm spot with a fluence of 1 mJ/mm^2. The laser hit the capillary from the side with its long axis parallel to the x-ray beam (60 μm by 100 μm) incoming direction. The x-ray beam generated from an in-vacuum undulator had an energy bandwidth $\Delta E/E = 3\%$ and a peak energy of 17.5 keV. The sample-to-detector distance was 400 mm, and a helium-filled conical chamber was placed in between the sample and the detector to reduce the background scattering from air. X-ray pulses with a 20-μs duration were isolated from the synchrotron in multibunch mode using a high-speed rotating chopper. The temperature in the experimental hutch was 294 K.

Each experiment generated data at one particular time delay between laser flash and x-ray pulse. A satisfactory signal-to-noise was achieved after measuring each time point ~1000 times. To avoid experimental drift in the measurements, time delays were recorded in a predefined order and interspersed with a negative time delay after three time delays: −50 μs, 20 μs, 10 ms, 100 ms, −50 μs, 5 ms, 1 ms, 20 ms, −50 μs, 50 ms, 2 ms, and 200 ms. Hence, the resulting time series was 20 μs, 1 ms, 2 ms, 5 ms, 10 ms, 20 ms, 50 ms, 100 ms, and 200 ms. The intensity of the scattered x-rays was recorded on a charge-coupled device (CCD) camera using 20-μs x-ray pulses, and 40 pulses were accumulated before each detector readout. The time series was repeated 27 times, and the difference scattering profiles are, hence, averages from 1080 measurements, which required a total amount of 20 mg of SR membranes. The experiments were performed with a 1-Hz repetition rate, ensuring that the sample was completely replenished in-between cycles. Because the obtained TR-XSS data also contain the solvent response to heating (*45*), these effects were removed according to a previous protocol (*23*) (fig. S1C). Control experiments of buffer or caged ATP in buffer showed no apparent difference intensities at 10 and 200 ms (fig. S6, D and E).

Data reduction

The recorded XSS images were azimuthally integrated to obtain radial intensity curves $S(\mathbf{q}, \Delta t)$ as a function of the magnitude of the scattering vector $\mathbf{q} = 4\pi\sin\theta/\lambda$, where 2θ is the angle of deflection, λ is the x-ray wavelength, and Δt is the time delay between the photoactivating laser pulse and the x-ray probe pulse. To obtain the difference spectra, −50 μs "dark" references were subtracted from each spectrum after normalization in a $\mathbf{q}$ region of 2.0 to 2.1 $Å^{-1}$, where minimal differences are expected. Difference data that diverged by more than 3.5 times the SD for the given time delay were considered as outliers and were excluded from further analysis. This resulted in

at least 85% of the data for each time point being retained. Hence, the obtained difference scattering curves only contain signals from the structural rearrangements in the sample.

SVD analysis

The TR-XSS dataset was arranged into an $m \times n$ matrix comprising difference scattering intensities recorded at 799 (m) $\mathbf{q}$ values and 9 (n) time points and decomposed using SVD according to the following equation

$$\Delta S(\mathbf{q}, \Delta t) = U(\mathbf{q})\, S_v\, V(\Delta t)^T \quad (1)$$

Here, $U(\mathbf{q})$ is an $m \times m$ matrix comprising the orthonormal basis spectra of the dataset ΔS. S_v is an $m \times n$ diagonal matrix indicating the contributions of the basis spectra (singular values), and $V(\Delta t)$ is an $n \times n$ matrix describing the time-dependent variation of the basis spectra. From this, the major signal-containing components in the dataset were determined. In agreement with the obtained SVD results that showed one dominating component (fig. S1, D and E), the peak amplitudes in the late basis spectrum were substantially larger compared with the early and intermediate spectra.

Spectral decomposition

To characterize the transient intermediates over time, kinetic models with an increasing number of states were used to describe the TR-XSS difference spectra. The SERCA difference scattering data from 0 to 2.35 Å^{-1} were spectrally decomposed according to sequential kinetic models

$$\text{Early} \xrightarrow{k_1} \text{Late}$$

$$\text{Early} \xrightarrow{k_1} \text{Intermediate} \xrightarrow{k_2} \text{Late}$$

where the rate constants correspond to the formation of transient states. The kinetic models assume irreversible steps and that the early states form concomitantly with the laser pulse. To obtain the time-independent basis spectra and rate constants associated with the formation of the transient structural intermediate states, we performed spectral decomposition with global fitting to the SERCA difference scattering data $S(\mathbf{q}, \Delta t)$ according to

$$\Delta S(\mathbf{q}, \Delta t)_{\text{theory}} = U_{\text{red}}(\mathbf{q})\, C(\Delta t) \quad (2)$$

where $U_{\text{red}}(\mathbf{q})$ is a $m \times k$ matrix containing the first k components, and $C(\Delta t)$ is a $k \times n$ matrix with the kinetic profiles for the k different transitions. The latter is given by the integrated rate equations

$$[\text{early}] = e^{-k_1 t} \quad (3)$$

$$[\text{intermediate}] = \frac{k_1}{k_2 - k_1}(e^{-k_1 t} - e^{-k_2 t}) \quad (4)$$

$$[\text{late}] = 1 + [(k_1 * e^{-k_2 t}) - (k_2 * e^{-k_1 t})]/(k_2 - k_1) \quad (5)$$

The rate constants were optimized by a global least squares refinement between the experimental and reconstituted data. To evaluate the agreement to the experimental data, linear combinations of the obtained basis spectra and corresponding population densities were fitted to the experimental difference data. The three-state model resulted in a better global least squares fit ($S = 1.9 \times 10^{-6}$; Fig. 2A) compared with the modeling transition between two states ($S = 2.9 \times 10^{-6}$), or decay of a single state ($S = 1.2 \times 10^{-5}$). The resulting basis spectra were subjected to a 10-point smoothening, which avoided experimental noise.

Structural refinement

Difference scattering curves were calculated using the software CRYSOL (*46*). Atomic and solvent-corrected difference profiles showed very similar features, but with solvent correction leading to slightly worse R-factors, which likely depends on that vesicles of intact SR membranes are not modeled well by assuming a water surrounding. Therefore, to avoid introducing an additional fitting parameter and possible overfitting to the experimental data, we used atomic scattering for comparisons that did not involve a membrane model. The SERCA crystal structure corresponding to a [Ca_2]E1 state (PDB ID: 2C9M) represented the initial prepulse "ground" state. Eight crystal structures were chosen as representatives for the principal SERCA intermediate states. All structures were modified to contain only protein and the same number of amino acid residues. The resulting calculated difference scattering profiles were corrected for the use of polychromatic radiation by convolution with the measured undulator spectrum. An R-factor was defined to measure the agreement between difference XSS curves predicted from structural models and the experimental difference scattering data in the $0 < \mathbf{q} < 0.6$ Å^{-1} range

$$R = \frac{\Sigma\sqrt{(\Delta S^{\text{theory}} - c{*}\Delta S^{\text{experiment}})^2}}{\Sigma\sqrt{(c{*}\Delta S^{\text{experiment}})^2}} \quad (6)$$

Here, $\Delta S^{\text{experiment}}$ represents a difference XSS basis spectrum from the spectral decomposition of the experimental data, ΔS^{theory} represents a calculated difference XSS curve from a given structural model, and c is the scaling factor that is allowed to vary to enable comparison between detector readout and CRYSOL calculations. To benchmark thermal protein dynamics at room temperature (i.e., minimum R-factor), the target difference spectra were obtained from the first and last frames in a Targeted Molecular Dynamics (TMD) simulation. The 0.1 R-factor was calculated on the basis of the dynamics displayed after the full transition, i.e., when the protein is biased toward the target structure and, hence, explores dynamics without moving toward a different state.

Targeted MD simulations

A crystal structure corresponding to a [Ca_2]E1 state (PDB ID: 2C9M) was centered in a simulation box with dimensions 200 Å by 200 Å by 200 Å and solvated by TIP3P waters using CHARMM-GUI (*47*) and relaxed in a 5000-step steepest descent energy minimization in the GROMACS 5.1.4 simulation package (*48*), followed by a short 25-ps constant number (N), volume (V), and temperature (T) (NVT) equilibration with a 1-fs timestep at a temperature of 303.15 K maintained by a Nose-Hoover temperature-coupling scheme (*49*, *50*). Force field parameters were described by the CHARMM36 additive force field for proteins (*51*). In seven targeted MD simulations, the [Ca_2]E1 state was driven toward each of the following states (and crystal structures): [Ca_2]E1ATP (PDB ID: 3N8G), [Ca_2]E1P-ADP (PDB ID: 1T5T), [Ca_2]E1P:ADP (PDB ID: 3BA6), E2P (PDB ID: 3B9B), E2-P

(PDB ID: 3N5K), E2:Pi (PDB ID: 3FGO), and E2 (PDB ID: 3NAL). The TMD simulations used the RMSD collective variable from Plugin for Molecular Dynamics (PLUMED) (*52*). The 10-ns trajectories used a Parrinello-Rahman pressure coupling (*53*, *54*) and Nose-Hoover thermostat (*49*, *50*). Protein coordinates were extracted every 100 ps, resulting in 100 structures per TMD trajectory and state. The calculated scattering from the $[Ca_2]$E1 state was then subtracted from each of those obtained from 100 protein structures distributed evenly throughout the transition trajectories to produce 100 difference scattering profiles.

Membrane-embedded MD simulations

The SR membrane containing 366 dimyristoylaminodeoxy phopshatidylcholine (DDPC), 138 palmitoyloleoyl phosphotidylethanolamine (POPE), 48 phosphatidylserine (POPS), 12 palmitoyloleoyl phosphotidylinositol (POPI), and 30 sphingomyelin (SM) lipids was created using the Membrane Builder (*55*) in CHARMM-GUI (*47*). The SERCA protein structures were inserted into the SR membrane model according to the Orientations of Protein in Membranes database (*56*). Force field parameters were described by a CHARMM36 additive force field for the protein (*51*) and lipids (*57*). Each simulation system was energy minimized with a 5000-step steepest descent method followed by gradually decreased restraints on protein and lipid heavy atoms for three consecutive 25-ps NVT simulations. In these simulations, a 1-fs timestep was used, and a temperature of 303.15 K was maintained using a Berendsen temperature-coupling scheme (*58*). This was followed by three consecutive 100-ps NPT simulations with further gradual release of heavy-atom restraints. In the last 100-ps simulation, the lipids were completely unrestrained and allowed to relax around the restrained protein. In these simulations, a 2-fs timestep was used, and the pressure was kept constant at one bar using a semi-isotropic Berendsen pressure barostat (*58*).

The protein conformations used in the structural refinement procedure were then produced in a 300-ns unrestrained simulation, one for each state. In these simulations, a 2-fs timestep was used, and the temperature was kept at 303.15 K with a Nose-Hoover thermostat (*49*, *50*) and a Parrinello-Rahman semi-isotropic barostat (*53*, *54*) was used to regulate pressure. A set of 200 protein structures were extracted from the unrestrained 2C9M (prepulse state) simulation and subtracted from each of the structures generated from the simulations of the transition models corresponding to intermediate and late states, respectively. The combination resulted in 40,000 difference profiles that were compared to the intermediate and late basis spectra.

Because SERCA transport structural dynamics are dominated by large conformational changes in the soluble domains protruding from the membrane, the influence from the surrounding lipids on the difference scattering should be negligible. To test whether including scattering cross-terms to the surrounding lipids and excluded solvent could alter the structural interpretation, we simulated disorder from a single SR membrane patch by calculating difference scattering $dS(\mathbf{q})$ profiles including a 200-$Å^2$ Debye-Waller B factor as previously described (*27*, *59*).

Statistical analysis

To estimate errors when describing localization of the cytoplasmic domains, we selected 10 prepulse, intermediate, and late-state structures from the membrane simulation trajectories that scored best in terms of R-factor to the experimental intermediate and late basis spectra. The R-factors were within 0.05 from the best fit. The RMSDs of the A, P, N, and M domains were calculated with respect to those of the representative crystal structures of $[Ca_2]$E1, $[Ca_2]$E1P:ADP, E2P, and E2-P states (PDB IDs: 2C9M, 3BA6, 3B9B, and 3N5K). The means and SDs of the calculated domain RMSD for the 10 pairs are reported in table S3.

SUPPLEMENTARY MATERIALS

Supplementary material for this article is available at http://advances.sciencemag.org/cgi/content/full/6/12/eaaz0981/DC1

Fig. S1. Data analyses and targeted MD approach.
Fig. S2. Targeted MD of E1 states.
Fig. S3. Reaction scheme and sequential x-ray scattering differences.
Fig. S4. Targeted MD of E2 states.
Fig. S5. R-factor analyses of the membrane simulations and pre-pulse TR-XSS models.
Fig. S6. Solvent and membrane scattering contributions and control TR-XSS experiments.
Table S1. Generating difference scattering using linear combinations of calculated scattering from crystal structures of putative prepulse states.
Table S2. Crystal structures (and PDB IDs) corresponding to principal transient enzymatic states in the SERCA reaction cycle considered in the structural refinement.
Table S3. Structural similarity (RMSD) between domains.
Table S4. List of abbreviations.

View/request a protocol for this paper from *Bio-protocol*.

REFERENCES AND NOTES

1. S. Ebashi, M. Endo, I. Otsuki, Control of muscle contraction. *Q. Rev. Biophys.* **2**, 351–384 (1969).
2. A. Zarain-Herzberg, G. García-Rivas, R. Estrada-Avilés, Regulation of SERCA pumps expression in diabetes. *Cell Calcium* **56**, 302–310 (2014).
3. A. M. Mata, M. R. Sepúlveda, Calcium pumps in the central nervous system. *Brain Res. BRev.* **49**, 398–405 (2005).
4. W. Kühlbrandt, Biology, structure and mechanism of P-type ATPases. *Nat. Rev. Mol. Cell Biol.* **5**, 282–295 (2004).
5. M. Periasamy, A. Kalyanasundaram, SERCA pump isoforms: Their role in calcium transport and disease. *Muscle Nerve* **35**, 430–442 (2007).
6. C. Toyoshima, How Ca^{2+}-ATPase pumps ions across the sarcoplasmic reticulum membrane. *Biochim. Biophys. Acta* **1793**, 941–946 (2009).
7. J. V. Møller, C. Olesen, A.-M. L. Winther, P. Nissen, The sarcoplasmic Ca^{2+}-ATPase: Design of a perfect chemi-osmotic pump. *Q. Rev. Biophys.* **43**, 501–566 (2010).
8. M. Andersson, E. Malmerberg, S. Westenhoff, G. Katona, M. Cammarata, A. B. Wöhri, L. C. Johansson, F. Ewald, M. Eklund, M. Wulff, J. Davidsson, R. Neutze, Structural dynamics of light-driven proton pumps. *Structure* **17**, 1265–1275 (2009).
9. J. Heberle, T. Gensch, When FT-IR spectroscopy meets x-ray crystallography. *Nat. Struct. Biol.* **8**, 195–197 (2001).
10. L. Herbette, J. K. Blasie, P. Defoor, S. Fleischer, R. J. Bick, W. B. Van Winkle, C. A. Tate, M. L. Entman, Phospholipid asymmetry in the isolated sarcoplasmic reticulum membrane. *Arch. Biochem. Biophys.* **234**, 235–242 (1984).
11. M. Dyla, S. Basse Hansen, P. Nissen, M. Kjaergaard, Structural dynamics of P-type ATPase ion pumps. *Biochem. Soc. Trans.* **47**, 1247–1257 (2019).
12. M. Liu, A. Barth, Mapping interactions between the Ca^{2+}-ATPase and its substrate ATP with infrared spectroscopy. *J. Biol. Chem.* **278**, 10112–10118 (2003).
13. C. Toyoshima, S. Iwasawa, H. Ogawa, A. Hirata, J. Tsueda, G. Inesi, Crystal structures of the calcium pump and sarcolipin in the Mg^{2+}-bound E1 state. *Nature* **495**, 260–264 (2013).
14. A.-M. L. Winther, M. Bublitz, J. L. Karlsen, J. V. Møller, J. B. Hansen, P. Nissen, M. J. Buch-Pedersen, The sarcolipin-bound calcium pump stabilizes calcium sites exposed to the cytoplasm. *Nature* **495**, 265–269 (2013).
15. S. Danko, T. Daiho, K. Yamasaki, X. Liu, H. Suzuki, Formation of the stable structural analog of ADP-sensitive phosphoenzyme of Ca^{2+}-ATPase with occluded Ca^{2+} by beryllium fluoride: Structural changes during phosphorylation and isomerization. *J. Biol. Chem.* **284**, 22722–22735 (2009).
16. M. Dyla, D. S. Terry, M. Kjaergaard, T. L.-M. Sørensen, J. L. Andersen, J. P. Andersen, C. R. Knudsen, R. B. Altman, P. Nissen, S. C. Blanchard, Dynamics of P-type ATPase transport revealed by single-molecule FRET. *Nature* **551**, 346–351 (2017).
17. S. Wakabayashi, M. Shigekawa, Role of divalent cation bound to phosphoenzyme intermediate of sarcoplasmic reticulum ATPase. *J. Biol. Chem.* **259**, 4427–4436 (1984).
18. J. E. Mahaney, D. D. Thomas, J. P. Froehlich, The time-dependent distribution of phosphorylated intermediates in native sarcoplasmic reticulum Ca^{2+}-ATPase from skeletal muscle is not compatible with a linear kinetic model. *Biochemistry* **43**, 4400–4416 (2004).
19. G. Meissner, G. E. Conner, S. Fleischer, Isolation of sarcoplasmic reticulum by zonal centrifugation and purification of Ca^{2+}-pump and Ca^{2+}-binding proteins. *Biochim. Biophys. Acta* **298**, 246–269 (1973).

20. J. K. Blasie, L. G. Herbette, D. Pascolini, V. Skita, D. H. Pierce, A. Scarpa, Time-resolved x-ray diffraction studies of the sarcoplasmic reticulum membrane during active transport. *Biophys. J.* **48**, 9–18 (1985).
21. J. Vincent, M. Andersson, M. Eklund, A. B. Wöhri, M. Odelius, E. Malmerberg, Q. Kong, M. Wulff, R. Neutze, J. Davidsson, Solvent dependent structural perturbations of chemical reaction intermediates visualized by time-resolved x-ray diffraction. *J. Chem. Phys.* **130**, 154502 (2009).
22. I. Josts, S. Niebling, Y. Gao, M. Levantino, H. Tidow, D. Monteiro, Photocage-initiated time-resolved solution x-ray scattering investigation of protein dimerization. *IUCrJ* **5**, 667–672 (2018).
23. M. Cammarata, M. Levantino, F. Schotte, P. A. Anfinrud, F. Ewald, J. Choi, A. Cupane, M. Wulff, H. Ihee, Tracking the structural dynamics of proteins in solution using time-resolved wide-angle x-ray scattering. *Nat. Methods* **5**, 881–886 (2008).
24. H. Takala, A. Björling, O. Berntsson, H. Lehtivuori, S. Niebling, M. Hoernke, I. Kosheleva, R. Henning, A. Menzel, J. A. Ihalainen, S. Westenhoff, Signal amplification and transduction in phytochrome photosensors. *Nature* **509**, 245–248 (2014).
25. A. Björling, O. Berntsson, H. Lehtivuori, H. Takala, A. J. Hughes, M. Panman, M. Hoernke, S. Niebling, L. Henry, R. Henning, I. Kosheleva, V. Chukharev, N. V. Tkachenko, A. Menzel, G. Newby, D. Khakhulin, M. Wulff, J. A. Ihalainen, S. Westenhoff, Structural photoactivation of a full-length bacterial phytochrome. *Sci. Adv.* **2**, e1600920 (2016).
26. O. Berntsson, R. P. Diensthuber, M. R. Panman, A. Björling, E. Gustavsson, M. Hoernke, A. J. Hughes, L. Henry, S. Niebling, H. Takala, J. A. Ihalainen, G. Newby, S. Kerruth, J. Heberle, M. Liebi, A. Menzel, R. Henning, I. Kosheleva, A. Möglich, S. Westenhoff, Sequential conformational transitions and alpha-helical supercoiling regulate a sensor histidine kinase. *Nat. Commun.* **8**, 284 (2017).
27. E. Malmerberg, Z. Omran, J. S. Hub, X. Li, G. Katona, S. Westenhoff, L. C. Johansson, M. Andersson, M. Cammarata, M. Wulff, D. van der Spoel, J. Davidsson, A. Specht, R. Neutze, Time-resolved WAXS reveals accelerated conformational changes in iodoretinal-substituted proteorhodopsin. *Biophys. J.* **101**, 1345–1353 (2011).
28. E. Malmerberg, P. H. M. Bovee-Geurts, G. Katona, X. Deupi, D. Arnlund, C. Wickstrand, L. C. Johansson, S. Westenhoff, E. Nazarenko, G. F. X. Schertler, A. Menzel, W. J. de Grip, R. Neutze, Conformational activation of visual rhodopsin in native disc membranes. *Sci. Signal.* **8**, ra26 (2015).
29. M. Andersson, J. Vincent, D. van der Spoel, J. Davidsson, R. Neutze, A proposed time-resolved x-ray scattering approach to track local and global conformational changes in membrane transport proteins. *Structure* **16**, 21–28 (2008).
30. M. Levantino, B. A. Yorke, D. C. F. Monteiro, M. Cammarata, A. R. Pearson, Using synchrotrons and XFELs for time-resolved x-ray crystallography and solution scattering experiments on biomolecules. *Curr. Opin. Struct. Biol.* **35**, 41–48 (2015).
31. A. Barth, K. Hauser, W. Mäntele, J. E. T. Corrie, D. R. Trentham, Photochemical release of ATP from "Caged ATP" studied by time-resolved infrared spectroscopy. *J. Am. Chem. Soc.* **117**, 10311–10316 (1995).
32. S. Verjovski-Almeida, M. Kurzmack, G. Inesi, Partial reactions in the catalytic and transport cycle of sarcoplasmic reticulum ATPase. *Biochemistry* **17**, 5006–5013 (1978).
33. U. Rasmussen, S. Brøogger Christensen, F. Sandberg, Thapsigargine and thapsigargicine, two new histamine liberators from Thapsia garganica L. *Acta Pharm. Suec.* **15**, 133–140 (1978).
34. J. P. Froehlich, E. W. Taylor, Transient state kinetic studies of sarcoplasmic reticulum adenosine triphosphatase. *J. Biol. Chem.* **250**, 2013–2021 (1975).
35. S. R. Midtgaard, T. A. Darwish, M. C. Pedersen, P. Huda, A. H. Larsen, G. V. Jensen, S. A. R. Kynde, N. Skar-Gislinge, A. J. Z. Nielsen, C. Olesen, M. Blaise, J. J. Dorosz, T. S. Thorsen, R. Venskutonytė, C. Krintel, J. V. Møller, H. Frielinghaus, E. P. Gilbert, A. Martel, J. S. Kastrup, P. E. Jensen, P. Nissen, L. Arleth, Invisible detergents for structure determination of membrane proteins by small-angle neutron scattering. *FEBS J.* **285**, 357–371 (2018).
36. Y. Sonntag, M. Musgaard, C. Olesen, B. Schiøtt, J. V. Møller, P. Nissen, L. Thøgersen, Mutual adaptation of a membrane protein and its lipid bilayer during conformational changes. *Nat. Commun.* **2**, 304 (2011).
37. C. Olesen, M. Picard, A.-M. L. Winther, C. Gyrup, J. P. Morth, C. Oxvig, J. V. Møller, P. Nissen, The structural basis of calcium transport by the calcium pump. *Nature* **450**, 1036–1042 (2007).
38. C. Toyoshima, M. Nakasako, H. Nomura, H. Ogawa, Crystal structure of the calcium pump of sarcoplasmic reticulum at 2.6 A resolution. *Nature* **405**, 647–655 (2000).
39. M. Shigekawa, S. Wakabayashi, H. Nakamura, Effect of divalent cation bound to the ATPase of sarcoplasmic reticulum. Activation of phosphoenzyme hydrolysis by Mg^{2+}. *J. Biol. Chem.* **258**, 14157–14161 (1983).
40. M. Shigekawa, J. P. Dougherty, Reaction mechanism of Ca^{2+}-dependent ATP hydrolysis by skeletal muscle sarcoplasmic reticulum in the absence of added alkali metal salts. II. Kinetic properties of the phosphoenzyme formed at the steady state in high Mg^{2+} and low Ca^{2+} concentrations. *J. Biol. Chem.* **253**, 1451–1457 (1978).
41. Y. Nakamura, Y. Tonomura, Changes in affinity for calcium ions with the formation of two kinds of phosphoenzyme in the Ca^{2+},Mg^{2+}-dependent ATPase of sarcoplasmic reticulum. *J. Biochem.* **91**, 449–461 (1982).
42. A. G. Lee, How lipids affect the activities of integral membrane proteins. *Biochim. Biophys. Acta* **1666**, 62–87 (2004).
43. J. V. Moller, C. Olesen, Preparation of Ca^{2+}-ATPase1a Enzyme from Rabbit Sarcoplasmic Reticulum. *Methods Mol. Biol.* **1377**, 11–17 (2016).
44. M. Wulff, A. Plech, L. Eybert, R. Randler, F. Schotte, P. Anfinrud, The realization of sub-nanosecond pump and probe experiments at the ESRF. *Faraday Discuss.* **122**, 13–26 (2003).
45. P. Georgiou, J. Vincent, M. Andersson, A. B. Wöhri, P. Gourdon, J. Poulsen, J. Davidsson, R. Neutze, Picosecond calorimetry: Time-resolved x-ray diffraction studies of liquid CH_2Cl_2. *J. Chem. Phys.* **124**, 234507 (2006).
46. D. Svergun, C. Barberato, M. H. J. Koch, CRYSOL - a program to evaluate x-ray solution scattering of biological macromolecules from atomic coordinates. *J. Appl. Crystallogr.* **28**, 768–773 (1995).
47. S. Jo, T. Kim, V. G. Iyer, W. Im, CHARMM-GUI: A web-based graphical user interface for CHARMM. *J. Comput. Chem.* **29**, 1859–1865 (2008).
48. M. Abraham, T. Murtola, R. Schulz, S. Páll, J. C. Smith, B. Hess, E. Lindahl, GROMACS: High performance molecular simulations through multi-level parallelism from laptops to supercomputers. *SoftwareX* **1-2**, 19–25 (2015).
49. S. Nosé, A unified formulation of the constant temperature molecular dynamics methods. *J. Chem. Phys.* **81**, 511–519 (1984).
50. W. G. Hoover, Canonical dynamics: Equilibrium phase-space distributions. *Phys. Rev. A* **31**, 1695–1697 (1985).
51. R. B. Best, X. Zhu, J. Shim, P. E. M. Lopes, J. Mittal, M. Feig, A. D. MacKerell Jr., Optimization of the additive CHARMM all-atom protein force field targeting improved sampling of the backbone ϕ, ψ and side-chain χ_1 and χ_2 dihedral angles. *J. Chem. Theory Comput.* **8**, 3257–3273 (2012).
52. G. A. Tribello, M. Bonomi, D. Branduardi, C. Camilloni, G. Bussi, Plumed 2: New feathers for an old bird. *Comput. Phys. Commun.* **185**, 604–613 (2014).
53. S. Nosé, M. L. Klein, Constant pressure molecular dynamics for molecular systems. *Mol. Phys.* **50**, 1055–1076 (1983).
54. M. Parrinello, A. Rahman, Polymorphic transitions in single crystals: A new molecular dynamics method. *J. Appl. Phys.* **52**, 7182–7190 (1981).
55. E. L. Wu, X. Cheng, S. Jo, H. Rui, K. C. Song, E. M. Dávila-Contreras, Y. Qi, J. Lee, V. Monje-Galvan, R. M. Venable, J. B. Klauda, W. Im, CHARMM-GUI Membrane Builder toward realistic biological membrane simulations. *J. Comput. Chem.* **35**, 1997–2004 (2014).
56. M. A. Lomize, I. D. Pogozheva, H. Joo, H. I. Mosberg, A. L. Lomize, OPM database and PPM web server: Resources for positioning of proteins in membranes. *Nucleic Acids Res.* **40**, D370–D376 (2012).
57. J. B. Klauda, R. M. Venable, J. A. Freites, J. W. O'Connor, D. J. Tobias, C. Mondragon-Ramirez, I. Vorobyov, A. D. MacKerell Jr., R. W. Pastor, Update of the CHARMM all-atom additive force field for lipids: Validation on six lipid types. *J. Phys. Chem. B* **114**, 7830–7843 (2010).
58. H. J. C. Berendsen, J. P. M. Postma, W. F. van Gunsteren, A. Dinola, J. R. Haak, Molecular dynamics with coupling to an external bath. *J. Chem. Phys.* **81**, 3684–3690 (1984).
59. E. Malmerberg, Conformational Dynamics of Rhodopsins Visualized by Time-resolved Wide Angle X-ray Scattering, thesis (2011).

Acknowledgments

Funding: This work was supported by Stiftelsen Olle Engkvist Byggmästare (2015/768) to H.R., an IWT doctoral scholarship provided by Agentschap Innoveren & Ondernemen (VLAIO) to A.S., the Lundbeck Foundation through the BRAINSTRUC (R328-2019-546) and DANDRITE (R248-2016-2518) centers to P.N., and a Swedish Research Council Starting Grant (2016-03610), Marie Curie Career Integration Grant (FP7-MC-CIG-618558), Magnus Bergvalls Stiftelse (2016-01593), and Åke Wibergs Stiftelse (M16-0164) to M.A. The computations were performed on resources provided by the Swedish National Infrastructure for Computing (SNIC) through the High-Performance Computing Center North (HPC2N) under project SNIC 2018/2-32. A.D. was co-funded by the William Harvey International Translational Research Academy and has received funding from the European Union's Seventh Framework Programme for research, technological development and demonstration activities under grant agreement no. 608765. **Author contributions:** M.A. conceived and designed the study. H.R., M.N.P., M.E., A.S., C.L., A.D., M.L., and M.A. performed the synchrotron experiments at ESRF with support from the ID09 beamline–responsible M.W. H.R. performed simulations. H.R., M.N.P., A.B., P.N., and M.A. analyzed the data. C.O. and P.N. supplied the sample. All authors contributed to the writing of the manuscript. **Competing interests:** The authors declare that they have no competing interests. **Data and materials availability:** All data needed to evaluate the conclusions in the paper are present in the paper and/or the Supplementary Materials. Additional data related to this paper may be requested from the authors.

Submitted 12 August 2019
Accepted 23 December 2019
Published 20 March 2020
10.1126/sciadv.aaz0981

Citation: H. Ravishankar, M. N. Pedersen, M. Eklund, A. Sitsel, C. Li, A. Duelli, M. Levantino, M. Wulff, A. Barth, C. Olesen, P. Nissen, M. Andersson, Tracking Ca^{2+} ATPase intermediates in real time by x-ray solution scattering. *Sci. Adv.* **6**, eaaz0981 (2020).

Science Advances

Tracking Ca^{2+} ATPase intermediates in real time by x-ray solution scattering

Harsha Ravishankar, Martin Nors Pedersen, Mattias Eklund, Aljona Sitsel, Chenge Li, Annette Duelli, Matteo Levantino, Michael Wulff, Andreas Barth, Claus Olesen, Poul Nissen and Magnus Andersson

Sci Adv **6** (12), eaaz0981.
DOI: 10.1126/sciadv.aaz0981